Journal of Taibah University for Science

ISSN: (Print) (Online) Journal homepage: https://www.tandfonline.com/loi/tusc20

Absorption of electromagnetic waves in sandstone saturated with brine and nanofluids for application in enhanced oil recovery

Hassan Ali , Hassan Soleimani , Noorhana Yahya , Shelley Lorimer , Maziyar Sabet , Birol M. R. Demiral & Lawal Lanre Adebayo

To cite this article: Hassan Ali , Hassan Soleimani , Noorhana Yahya , Shelley Lorimer , Maziyar Sabet , Birol M. R. Demiral & Lawal Lanre Adebayo (2020) Absorption of electromagnetic waves in sandstone saturated with brine and nanofluids for application in enhanced oil recovery, Journal of Taibah University for Science, 14:1, 217-226, DOI: 10.1080/16583655.2020.1718467

To link to this article: https://doi.org/10.1080/16583655.2020.1718467

© 2020 The Author(s). Published by Informa UK Limited, trading as Taylor & Francis Group

Published online: 26 Jan 2020.

Submit your article to this journal

Article views: 1016

View related articles

View Crossmark data

Citing articles: 6 View citing articles

Full Terms & Conditions of access and use can be found at
https://www.tandfonline.com/action/journalInformation?journalCode=tusc20

JOURNAL OF TAIBAH UNIVERSITY FOR SCIENCE
2020, VOL. 14, NO. 1, 217–226
https://doi.org/10.1080/16583655.2020.1718467

JTUSCI

Journal of Taibah University for Science

Taylor & Francis
Taylor & Francis Group

RESEARCH ARTICLE

OPEN ACCESS Check for updates

Absorption of electromagnetic waves in sandstone saturated with brine and nanofluids for application in enhanced oil recovery

Hassan Ali [a], Hassan Soleimani [a], Noorhana Yahya [a], Shelley Lorimer [b], Maziyar Sabet [c], Birol M. R. Demiral [d] and Lawal Lanre Adebayo [a]

[a]Fundamental and Applied Sciences Department, Universiti Teknologi Petronas, Bandar Seri Iskandar, Malaysia; [b]Department of Mathematics and Statistics, MacEwan Universiti, Edmonton, Canada; [c]Department of Petroleum and Chemical Engineering, Jalan Tungku Link, Darussalam, Brunei; [d]Schlumberger NExT, Dubai, UAE

ABSTRACT

In this study, scattering parameters of sandstone saturated with brine and nanofluids are evaluated experimentally and numerically for the application in enhanced oil recovery (EOR). Zinc Oxide (ZnO) and Bismuth ferrite $BiFeO_3$ (BFO) nanoparticles were synthesized via facile sol–gel method followed by nanofluid preparation. Sandstone samples were saturated with brine and nanofluids for 48 h. Electromagnetic properties of the saturated sandstones were measured experimentally using the vector network analyzer, and the scattering parameters of the samples were studied numerically by finite element method. BFO displayed higher permeability value of 1.52 and 1.30, as well as superior dielectric permittivity value 11.55 and 6.59 for real and imaginary parts, respectively. In addition, the sandstone saturated with BFO showed an impressive reflection loss (RL) value of −9.77 dB at high frequency. Conclusively, $BiFeO_3$ nanofluids showed the best potential to enhance oil recovery which can be accredited to the superior electromagnetic properties of BFO.

ARTICLE HISTORY
Received 31 October 2019
Revised 13 January 2020
Accepted 14 January 2020

KEYWORDS
Electromagnetic waves; porous rock; nanofluid; enhanced oil recovery

Nomenclature

μ_r	Relative permeability ($N{\cdot}A^{-2}$)
ε_r	Relative permittivity ($F{\cdot}m^{-1}$)
k_0	Wave number (m^{-1})
ϵ_0	Permittivity in free space ($=8.85E{-}12\ F{\cdot}m^{-1}$)
n	Refractive index
E	Electric displacement field ($C{\cdot}m^{-2}$)
RL	Reflection loss (dB)
Z	Input impedance (Ω)
J	Complex number
f_0	Applied frequency (Hz)
c	Speed of light (m/s)
t	Thickness (m)
μ'	Real part calculated permeability
μ''	Imaginary part calculated permeability
ε'	Real part calculated Dielectric permittivity
ε''	Imaginary part calculated dielectric permittivity
$\tan\delta_\mu$	Magnetic loss factor
$\tan\delta_\varepsilon$	Dielectric loss factor
S11	EM wave transmitted and received at port 1
S12	EM wave transmitted at port 1 and received at port 2

Abbreviations

S_0	Dry sandstone
S_B	Sandstone soaked in Brine
S_{Zn}	Sandstone soaked in ZnO nanofluid
S_{Bi}	Sandstone soaked in $BiFeO_3$ nanofluid
ε_s	Dielectric permittivity with sandstone
ε_B	Dielectric permittivity with Brine
ε_{Zn}	Dielectric permittivity with ZnO
ε_{Bi}	Dielectric permittivity with BiFeO3

Greek letters

Σ	Conductivity (S/m)
ω	Frequency (Hz)
λ	Wavelength (m)

1. Introduction

The global demand for energy is increasing and it is predicted to rise by 50% in 2030 [1]. Although renewable energy sources are being adopted to fulfil these energy needs, the oil will remain as the primary energy source for the next few decades [2]. So, along with the exploration of new oil fields, it is also necessary to maximize the production of oil from the existing oil fields [3,4]. Use of nanotechnology for enhanced oil recovery (EOR) has been gaining more attention of researchers as the nanoparticles can improve the rock-fluid properties such as wettability alteration, interfacial tension reduction, thermal conductivity, specific heat improvement,

CONTACT Hassan Ali hassan_ali87@hotmail.com Fundamental and Applied Sciences Department, Universiti Teknologi Petronas, Bandar Seri Iskandar, 32610 Perak, Malaysia

© 2020 The Author(s). Published by Informa UK Limited, trading as Taylor & Francis Group
This is an Open Access article distributed under the terms of the Creative Commons Attribution License (http://creativecommons.org/licenses/by/4.0/), which permits unrestricted use, distribution, and reproduction in any medium, provided the original work is properly cited.

and viscosity enhancement. Nanoparticles and nanofluids can accelerate the transfer rate of oil due to the migration of nanoparticles from the aqueous phase to the oleic phase affecting both the oil properties and rock oil properties to change [5–7]. For example, oil mobility may increase owing to the change in viscosity which may enhance the ultimate recovery of oil in fractured reservoirs.

Many researchers have used different categories of nanoparticles for EOR, such as the metal oxide nanoparticles [8,9], carbon-based nanoparticles [10–12], polymeric nanoparticles [13], and ferrite nanoparticles [14,15]. Kothari et al. for the first time flipped the term of "smart-nanofluids" when the ferrofluid was used as a surfactant for EOR, but the only the rheological properties of ferrofluids were studied [16]. Zinc Oxide (ZnO) has also been considered as a potential material for EOR because of its excellent dielectric properties and high dielectric loss in the presence of EM field [17]. To increase the activity of nanoparticles, electromagnetic waves of a specific frequency creates resonance in the nanoparticles changes the oil viscosity and compels to move inside the porous medium [18,19]. Various theoretical models were also proposed by researchers to describe the mechanisms involved in the chain-like formation, such as water-bridge model, electric double layer model and polarization model [20,21]. Later, among these models, has been considered as the most reliable model, which involves the dielectric loss to influence the electrorheological effect [22].

Ferrite nanocomposites have been of great interest in modern science and technology, which show substantial dielectric and magnetic properties [23,24]. They are not only known for their perspective of solid-state physics, but they have demonstrated a higher potential a variety of applications in electronic devices, wireless communications, medicine and industry [25–29]. Ferroic materials exhibit a unique property of spontaneously switching internal order of materials because of magneto-electric coupling, which results in the swapping of the magnetic field with electric polarization and vice versa [30]. This unique behaviour makes the ferrite nanocomposites favourable agent for EM-assisted EOR, which uses a novel class of smart nanofluids under the influence of electromagnetic field to stimulate them and create a disturbance at the oil–water interface [31–34]. The smart-nanofluids can drastically alter the viscosity, wettability and interfacial tension of oil–water; hence increasing the mobility of oil [35,36].

When the EM wave travels across an inhomogeneous material, it could change the material characteristics such as permittivity, permeability, conductivity, is, interference and phase-shift [37,38]. The absorption properties of such "smart-nanofluids" attribute to the reflection and transmission coefficients (S-Parameters) [19,39]. The dielectric materials can absorb the EM waves incident on them in synchronized frequencies which results in the polarization and the magneto-electric coupling and later dissipate the energy [40]. However, some of the disadvantages which restrict their broad applications are narrow EM frequency bandwidth, poor mechanical properties and low environmental adaptability [41,42]. The factors which affect the absorbing properties of materials are the materials complex permittivity ε'', complex permeability μ'' and dielectric losses δ [43]. In case of homogenous materials, the behaviour of wave can be measured analytically by using Fresnel equations and Snell's law, but for complex structures like sandstone numerical techniques are used for the calculation process, and a lot of programs have been used for realization of numerical modelling such as, MATLAB, ANSYS, COMSOL, etc [44].

In this work, synthesis of ZnO and $BiFeO_3$ nanoparticles was carried out using the sol–gel combustion technique. Then, nanofluids were prepared by dispersing the as-prepared nanoparticles in brine. Different samples of sandstone were saturated in nanofluids as well as brine. Subsequently, the magnetic and dielectric properties of the samples were measured with vector network analyzer (VNA). A numerical model based on the finite element method (FEM) was proposed to simulate the propagation of EM waves in multiphase porous media for the comparative analysis of experimental and simulation results.

2. Methodology

2.1. Synthesis of nanoparticles

ZnO nanoparticles were synthesized using zinc nitrate hexahydrate ($Zn(NO_3)_2{\cdot}6H_2O$) and NaOH solution, and the citric acid was used as a catalyst. The reaction was carried out using sol–gel combustion method by mixing 12 g of zinc nitrate hexahydrate in 100 ml of water in a beaker and 3.2 g of NaOH was dissolved in 30 ml of water in a separate beaker. Then the solution of NaOH added dropwise in the beaker and stirred for two hours at 70°C. The solution was then filtered with Whatman filter papers and dried in an oven for 3 h at 160°C, and later calcinated at 400°C for 3 h.

For bismuth ferrite (BFO) nanocomposite, bismuth nitrate pentahydrate ($Bi(NO_3)_2{\cdot}5H_2O$) and iron nitrate $Fe(NO_3)_2$ were used with nitric acid as an oxidizing agent. All the chemicals were purchased from Sigma Aldrich with analytical grade. BFO was synthesized by using solvent evaporation technique. Equal amounts of 0.1 M solutions of iron nitrate nonahydrate $Fe(NO_3)_3{\cdot}9H_2O$ and bismuth nitrate pentahydrate $Bi(NO_3)_3{\cdot}5H_2O$ were mixed, and dilute nitric acid was added as an oxidizing agent. The transparent solution was obtained by heating the mixture at 150–160°C under constant stirring until all the liquid evaporated from the solution. A green colour residual is obtained, which was grinned to make it a fine powder. The sample was annealed at

500°C for 2 h to remove the impurities to get single-phase BFO nanoparticles.

2.2. Nanofluid preparation

In a typical experiment, 0.1wt% of as-synthesized nanopartilces were dispersed in brine (3 wt% Nacl) as the basefluid, shown in Table 1. The solution was stirred for 1hour to achieve homogenous dispersion. The concentration and weight percent of NaCl and nanoparticles used in this work was adopted to avoid the agglomeration and favour better suspension [45]. The sandstone was cut perfectly with a size of $3 \times 4 \times 10$ mm so that it could be placed in the sample holder of the VNA. These sandstone samples were then dipped in the prepared solutions of brine, ZnO and BFO separately for 48 h so that it gets entirely saturated with nanofluids and brine, as shown in Figure 1.

2.3. Characterization of synthesized particles

X-ray diffraction (XRD) patterns obtained for the nanoparticles were carried out using powder X-ray diffractometer with Cu–Ka radiation operated at 45 kV and 40 ma [19]. The particle morphology and elemental analysis were carried out by Zeiss supra 55 VP FESEM [46].

Electromagnetic properties and microwave absorption were studied using a Keysight VNA at X-band frequencies. Dielectric and magnetic properties of lossless and lossy materials influence the electromagnetic field distribution. Relative permittivity ($\varepsilon = \varepsilon' - j\varepsilon''$) and relative permeability ($\mu = \mu' - j\mu$) defines the dielectric and magnetic properties of the materials, respectively, and influence the reflection of EM waves at the interfaces and the attenuation of the wave within the materials [43,47,48]. Here ε' and μ' are the real parts and express the energy stored in the material when the electromagnetic field is passed through it. Whereas, the complex quantities ε'' and μ'' defines the loss factor and influences the energy absorption and attenuation. Another critical parameter for dielectric properties of the material is the tangent of loss angle ($\tan\delta_\varepsilon = \varepsilon''/\varepsilon'$) and ($\tan\delta_\mu = \mu''/\mu'$), it contributes to the electromagnetic loss in heterogeneous media [49,50].

The measurement of frequency dependences of the real and complex relative permittivity of porous rocks saturated with brine and nanofluid is helpful for the petrophysical analysis of rocks for EOR. The rock samples were obtained from the Angsi-E2 and were soaked with brine, ZnO and BFO nanofluids, to saturate the rock. For simplicity, the samples were named as S_0, S_B, S_{Zn} and S_{Bi} for dry sandstone, and the sandstone saturated with brine, ZnO and BFO nanofluids, respectively. The measurements were carried out at X-Band frequency range of 8–12.5 GHz using the VNA. A VNA is a precision measuring tool that measures the dielectric properties of the materials as well as the reflection and transmission responses or S-Parameters. The rock samples were cut in the specific dimensions so that they can be placed in the sample holder without any gap. The network analyzer was calibrated using two-port transmission reflection line, and then after putting the frequency values the measurements were carried out.

Table 1. Concentration of salt and nanoparticles for the saturation of sandstone with brine and nanofluid.

Sample name	Nanoparticle	wt.% of Salt (NaCl)	wt.% of Nanoparticles
S_0	Sandstone	0	0
S_B	Brine	15	0
S_{Zn}	ZnO	3	0.1
S_{Bi}	BiFeO3	3	0.1

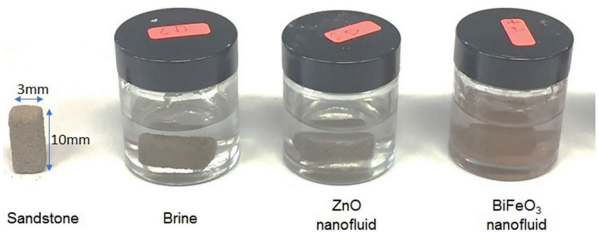

Figure 1. Experimental representation of the size of sandstone and the sandstone soaked in Brine, ZnO and BFO.

2.4. Numerical simulation

A numerical model based on the FEM has been adopted to solve the system of equations to describe the scattering parameters and propagation of EM waves across the sandstone just like in VNA system [51]. Two-port rectangular waveguide system was used in which Port 1 was for the incident wave, and Port 2 behaves as a receiver to study the reflection, transmission and losses of EM waves in the porous medium as shown in Figure 2.

$$\nabla \times \mu_r^{-1}(\nabla \times E) - k_o^2\left(\varepsilon_r - \frac{j\sigma}{\omega\epsilon_o}\right)E = 0. \quad (1)$$

In this model, the electromagnetic waves frequency domain interface with the rectangular waveguide Transverse electric (TE10) mode was used, and the two-port boundary conditions were selected for wave excitation. The other boundaries were specified with zero electric field conditions which are expressed as ($\hat{n} \times E = 0$), where $\hat{n}$ is the normal to the boundary [52]. The mesh dependence study was performed with respect to several computational meshes of various resolutions. A typical mesh consisting of 4932 total mesh vertices and 25748 tetrahedra elements in the entire domain.was selected for numerial investigations. The wave equation for the propagation of electric field "*E*" by solving the Maxwell equations is given as [53],

The wavenumber k_0 for free space is defined as [54],

$$k_0 = \omega\sqrt{\varepsilon_0\mu_0}. \quad (2)$$

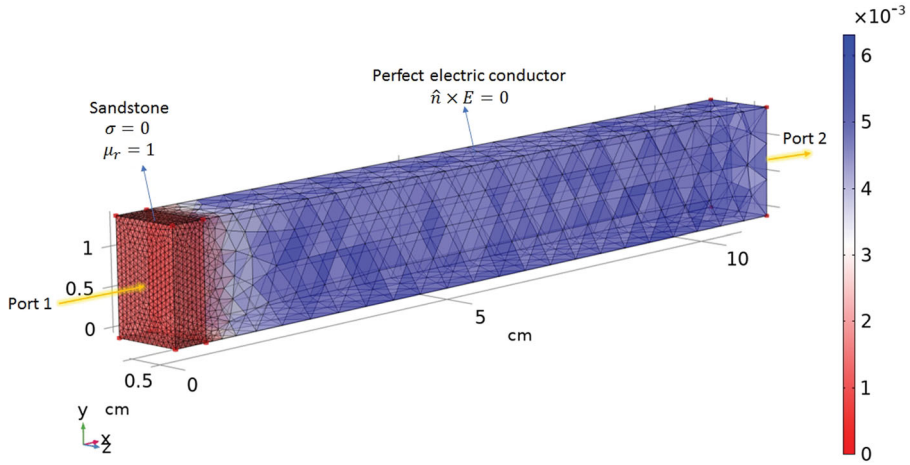

Figure 2. A simulation model of a porous medium with a two-port system.

Table 2. Input parameters for the mathematical model.

Description	Name	Value/expression
Relative permittivity of sandstone (S_0)	ε_S	3.966
Relative permittivity of sandstone with brine (S_B)	ε_B	5.6521
Relative permittivity of sandstone with ZnO (S_{Zn})	ε_{Zn}	10.119
Relative permittivity of sandstone with $BiFeO_3$ (S_{Bi})	ε_{Bi}	8.9344
Applied frequency	f_0	8.2 ~ 12.4 GHz

The electric displacement field model was selected for the refractive index, which was calculated using the permittivity and permeability values of the materials. The average values of relative permittivity for S_0, S_B, S_{Zn}, and S_{Bi} presented in Table 2 have been calculated using the measured values from VNA. By making the assumptions as $\sigma = 0$ and $\mu_r = 1$, we get Equation (1) in terms of refractive index as $\varepsilon_r = n^2$,

$$\nabla \times (\nabla \times E) - k_0^2 n^2 E = 0. \tag{3}$$

Scattering parameters (or S-parameters) describe the input and output parameters between two ports of an electrical system [55]. If we have a two-port system and each port is provided with some voltage and current, then S21 is defined as the power transferred from port 1–2, and S11 is the power transmitted and reflected at port 1 [56]. The simulations were carried separately for dry rock, the rock saturated with brine and nanofluids to study the reflection and transmission coefficients. The equations used for S-parameters at port 1 and port 2 are given in Equations (4) and (5), respectively [57].

$$S_{11} = \frac{\int_{port1} ((E - E_1) \cdot E_1) dA_1}{\int_{port1} (E_1 \cdot E_1) dA_1}, \tag{4}$$

$$S_{21} = \frac{\int_{port2} (E \cdot E_2) dA_2}{\int_{port2} (E_2 \cdot E_2) dA_1}. \tag{5}$$

Here the subscript 1 and 2 are for the port-1 and port-2, E is the electric field and A is the surface area. By using these equations, the reflection and transmission coefficients of the electromagnetic field have been calculated.

3. Results and discussion

3.1. XRD Analysis

The XRD patterns of ZnO nanoparticles calcinated at 400°C in Figure 3(a) shows that after calcination, very sharp peaks of ZnO were obtained and the other impurity peaks disappeared at high temperature. The main ZnO peaks were obtained at 2θ of 31.849° ($d = 2.8074$), 36.357° ($d = 2.4690$) and 68.16° ($d = 1.3754$) corresponding to (100), (101) and (2-10), respectively. The diffraction peaks in Figure 3(b) shows the formation of $BiFeO_3$ with hkl parameters (10-2), (104), (202), (2-16) and (412).

3.2. FESEM analysis

The morphology of ZnO and BFO nanoparticles were characterized using field emission scanning electron

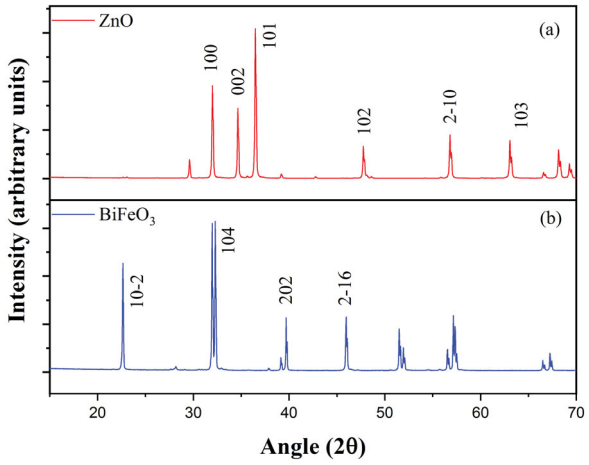

Figure 3. XRD pattern of (a) ZnO particles calcinated at 400°C (b) BFO nanoparticles calcinated at 500°C

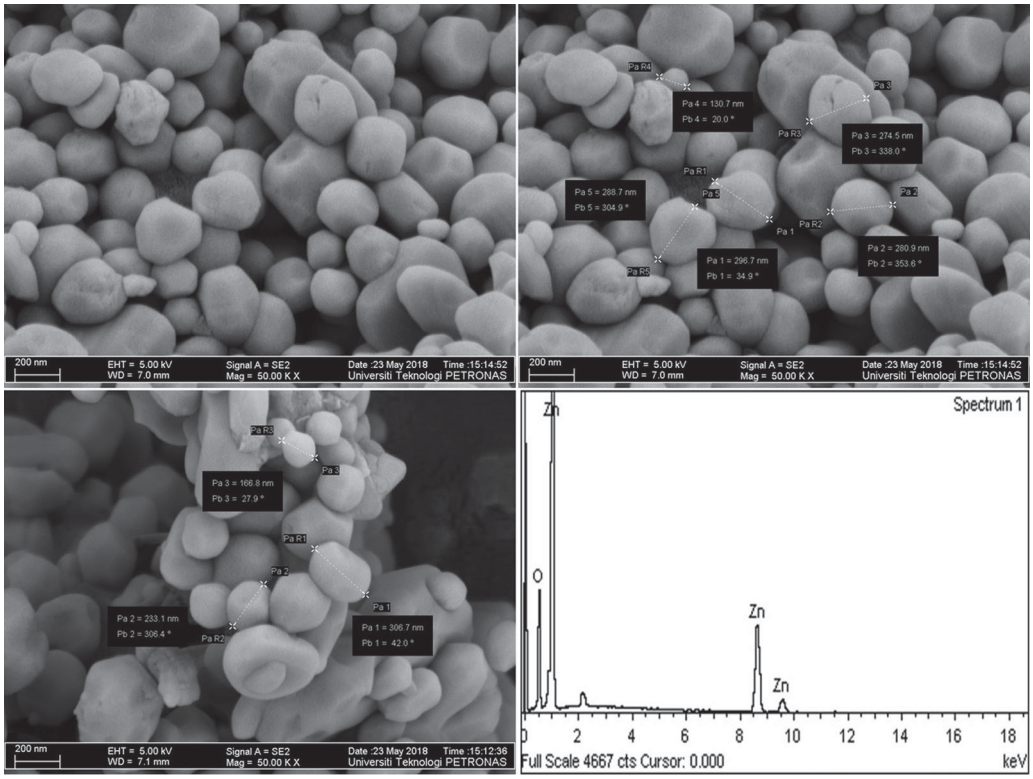

Figure 4. FESEM analysis of ZnO nanoparticles calcinated at 400°C.

microscope (FESEM). Energy dispersive X-ray (EDX) was also performed for nanoparticles, which confirmed the formation of ZnO and BFO. Figure 4 shows the micrographs of ZnO nanoparticles; the average size of the particles was above 150 nm because of the low calcination temperature and possible oxidation of nanoparticles. The shape of nanoparticles formed is hexagonal which is consistent with XRD results. The EDX results of ZnO shows that the zinc and oxygen elements are present with an atomic percentage of 36.41% and 63.59%. FESEM micrographs of BFO shown in Figure 5 was carried out at magnification of 30 KX. Nanoparticles got agglomerated and formed plane surfaces, which happened because of the oxidation at high temperature. The EDX analysis shows the atomic percentage of elements present are bismuth 20.37%, iron 20.49% and oxygen 59.14%.

FESEM micrographs of BFO shown in Figure 5 was carried out at magnification of 30 KX. Nanoparticles got agglomerated and formed plane surfaces, which happened because of the oxidation at high temperature. The EDX analysis shows the atomic percentage of elements present are bismuth 20.37%, iron 20.49% and oxygen 59.14%.

3.3. Measurement of EM wave absorption

The real part of dielectric permittivity (ε') is measured for all the samples at a range of frequencies 8.5–12.5 GHz as shown in Figure 6(a). The analysis of the dielectric permittivity dependence shows that S_{Bi} exhibits the maximum average value for dielectric permittivity ε'. This behaviour is due to the presence of additional relaxation due to the polarization of BFO nanoparticles in S_{Bi}. The samples S_0 and S_B show no variation until the frequency reached 9.5 GHz, after surpassing this frequency there is a rapid increase in dielectric permittivity, this abnormal change in behaviour occurs at that frequency range due to the effective conductivity dependence. Figure 6(b) shows the dielectric loss (ε'') with the X-band frequency for S_0, S_B, S_{Zn} and S_{Bi}. It is observed that the dielectric loss for S_{Bi} and S_{Zn} fall in the same range and is maximum for all the X-band frequencies. For S_0 and S_B the value of ε'' goes in the negative direction, which is an abnormal behaviour, the average value for these samples is zero. The dielectric loss as a function of frequency is increasing with the increasing frequency in S_{Bi}, which is due to the space charge polarization and reduced ionic conductivity. The variation of dielectric loss factor ($\tan\delta_\varepsilon$) with frequency for all the samples is shown in Figure 6(c). The $\tan\delta_\varepsilon$ is defined as the energy dissipation in dielectric media due to the domain wall resonance. As the value of ($\tan\delta_\varepsilon$) is directly proportional to ε'', it shows the same pattern as dielectric loss. The maximum loss factor at higher frequency is recorded for S_{Zn} and $S_{Bi,}$ which is due to the relaxation of ions.

Figure 7 represents the μ', μ'' and tan (δ_μ) as a function of X-band frequency. The value of μ' and μ'' are generally smaller in magnitude as compared to dielectric loss. For S_B and S_{Bi} the value of μ' does not vary much with increasing frequency, S_{Zn} shows a negative

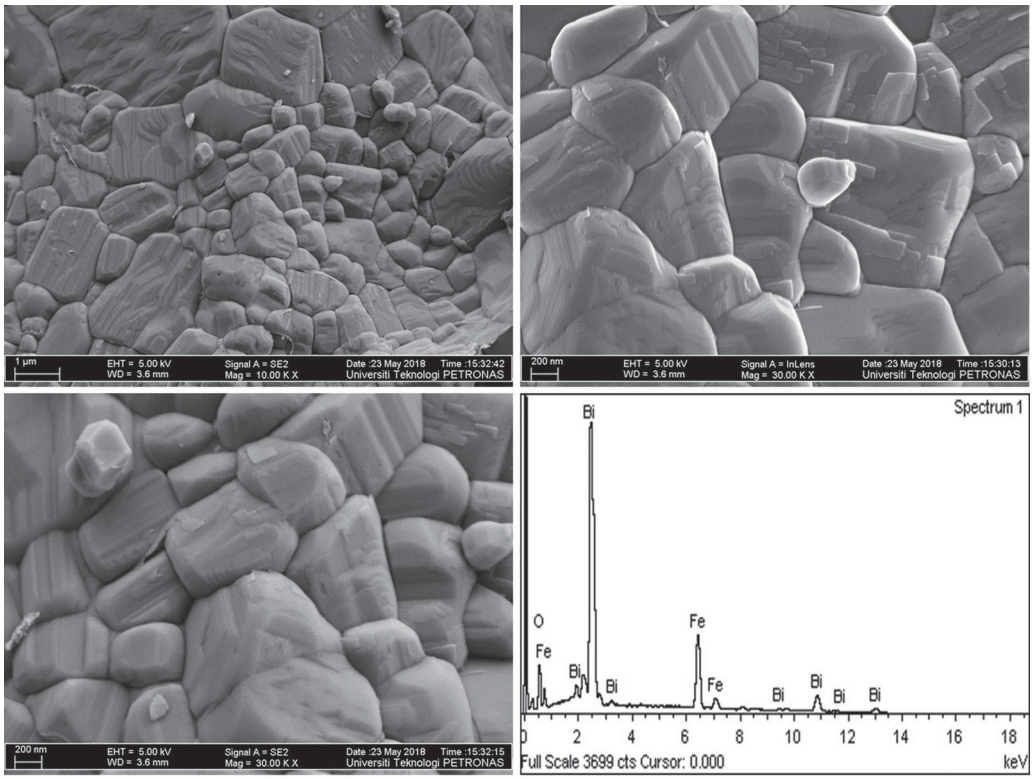

Figure 5. FESEM analysis of BFO calcinated at 500°C.

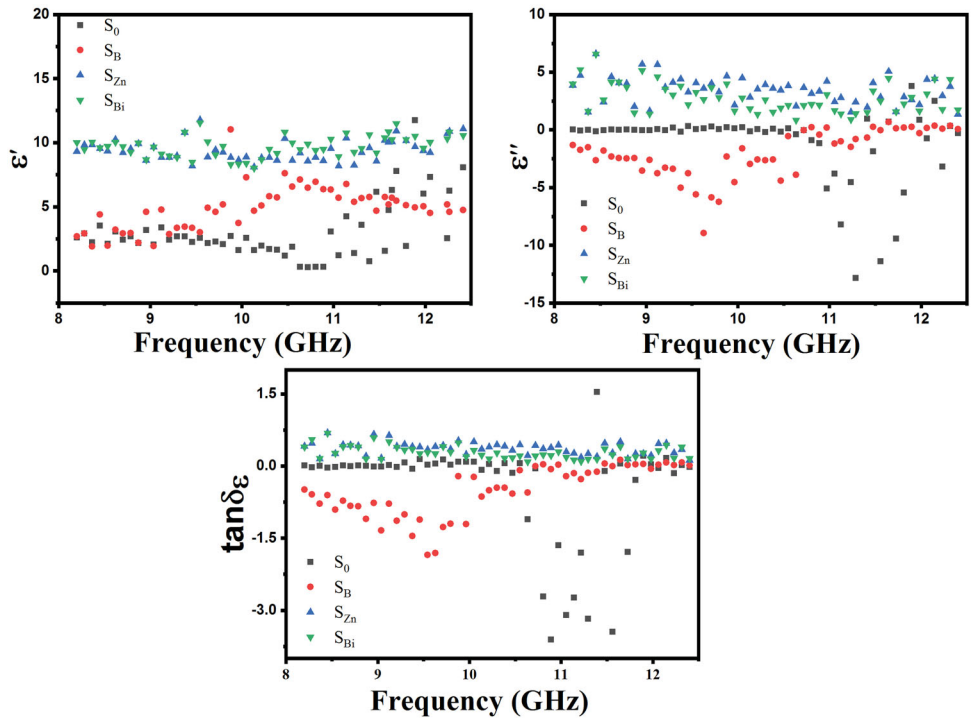

Figure 6. (a) Behaviour of dielectric permittivity (ε') as a function of frequency for S_0, S_B, S_{Zn}, and S_{Bi} (b) dielectric loss ε'' (c) dielectric loss factor (tanδ_ε).

trend and then increases slightly after 10 GHz because of the absence of magnetic properties of ZnO. S_{Bi} shows positive values of μ' as the permeability increases with increasing frequency. S_0 shows an abnormal behaviour after a frequency of 10 GHz. The imaginary part μ'' shows at the frequency of 8–9.5 GHz brine has the maximum magnetic loss while as the frequency increases S_{Bi} shows a positive trend for μ''. S_0 at a lower frequency, have zero magnetic loss, but with increasing frequency, it shows an abrupt increase and decrease in magnetic loss properties. Then there is magnetic loss factor tan(δ_μ) which is given by tan(δ_μ) = μ''/μ'. At frequency range of 8–10 GHz S_{Zn} have the highest tan(δ_μ), while at a frequency greater than 10 GHz, S_{Bi}

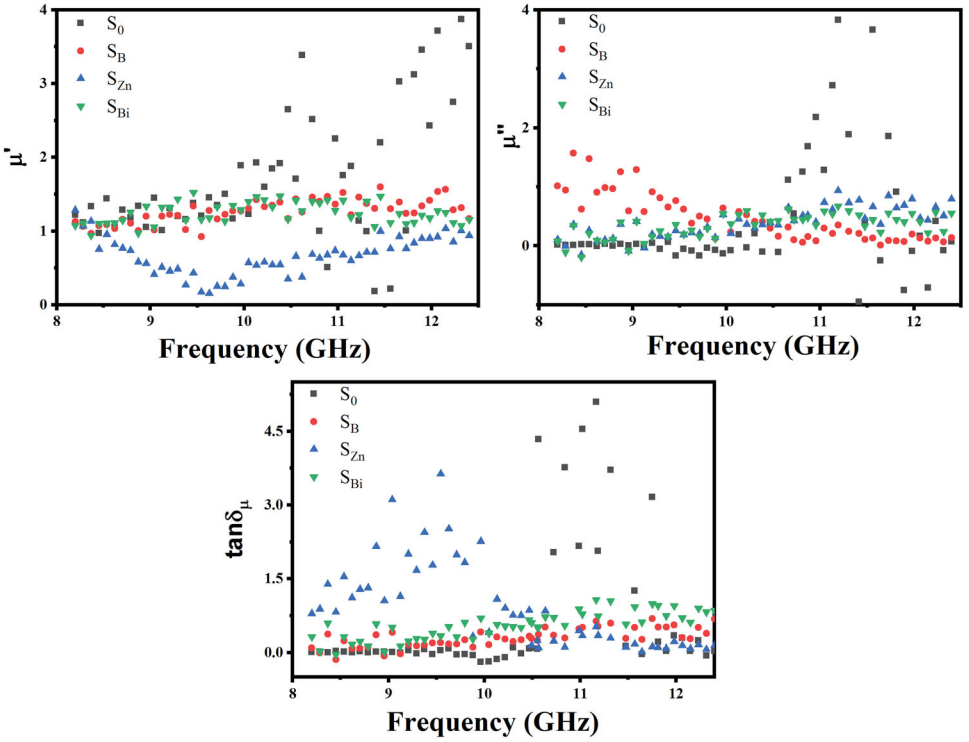

Figure 7. (a) Behaviour of permeability (μ') as a function of frequency for S_0, S_B, S_{Zn}, and S_{Bi} (b) imaginary part of permeability (μ'') (c) magnetic loss factor (tanδ_μ).

shows an increment in tangent loss factor. The magnetic loss occurs because of the domain wall resonance, natural resonance and eddy current loss. Domain wall resonance mainly occurs in the MHz frequency range, so in the microwave range, the S_{Bi} can be graded as the best material for absorbing EM waves and exhibit the natural resonance phenomenon.

3.4. Reflection loss

At the X-band frequency range based on the measurements of the scattering parameter, the reflection loss (RL) of all samples were calculated by using the absorbing wall theory,

$$Z = \sqrt{\frac{\mu}{\varepsilon}} \tan h \left(j \frac{2\pi f t}{c} \sqrt{\mu\varepsilon} \right), \tag{6}$$

$$\mathrm{RL} = 20 \log \left(\frac{Z-1}{Z+1} \right). \tag{7}$$

Here, RL donates the reflection loss in decibel units (dB), Z is the input impedance on the surface, ε and μ are the relative permittivity and permeability, j is the complex number, f is the frequency, c is the speed of light and t is the thickness of the sample used. RL curves outline the absorption coefficient of EM waves with a range of frequency correspond to RL value less than −10 dB correspond to 90% EM wave absorption. Figure 8 shows the variation of RL curves across the X-Band frequency range for S_0, S_B, S_{Zn}, and S_{Bi}. The most robust value for EM wave absorption was calculated for S_0 (−38 dB). For

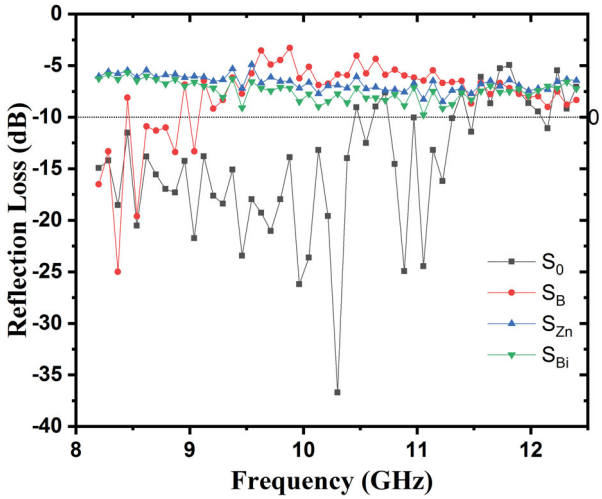

Figure 8. RL curves for S_0, S_B, S_{Zn}, and S_{Bi} at X-band (8.2–12.4 GHz) frequency.

S_B and S_{Bi}, the RL calculated was higher than −10 dB, except for S_{Zn}, which showed impressive absorption −25 dB at the relatively lower frequency of 8.35 GHz and the bandwidth of 0.8 4 GHz. S_{Bi} nanofluid exhibits the maximum absorption of −9.77 dB at a frequency of 11.05 GHz. The reason for high absorption in S_0 is the factors such as shape and size of the crystal, because of the porous structure the surface increases which is an essential factor for microwave absorbing materials. For all other samples, the pores of the sandstone were

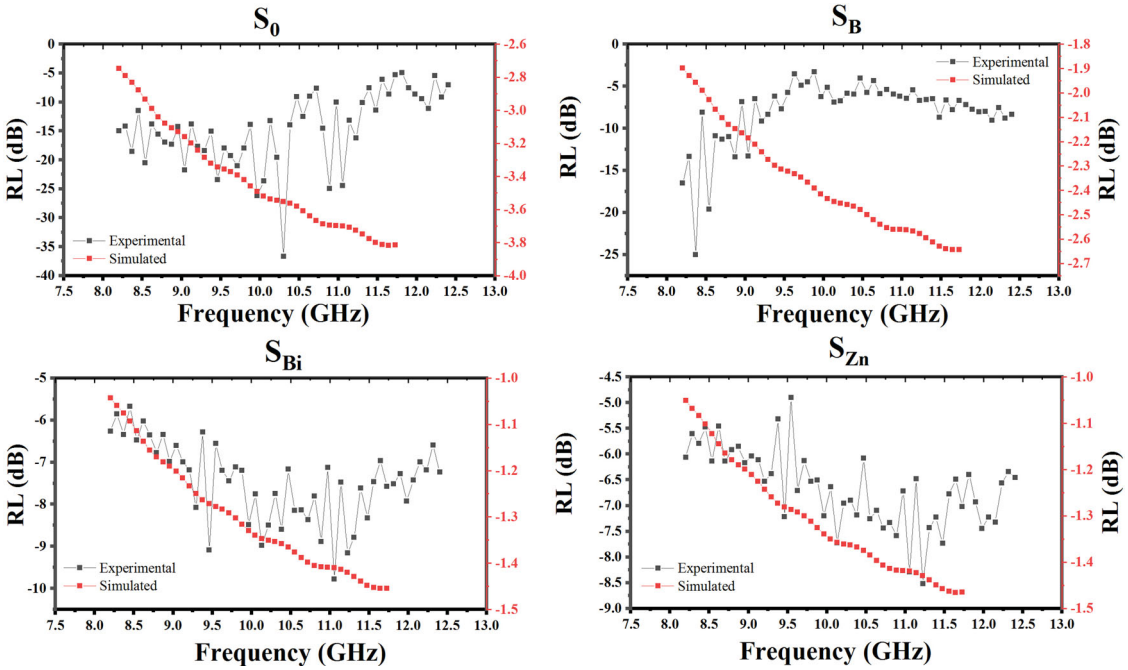

Figure 9. Comparison of the experimental and simulated results for RL (dB) at the X-band frequency range.

filled with brine or nanofluid; hence, the surface area decreases.

Numerical simulation of RL for sandstone, brine and nanofluids were carried out; all the materials show a decline in trend with increasing frequency, and the minimum RL is calculated for S_0 which means that most of the EM wave reflects from S_0. The RL for S_{Bi} and S_{Zn} recorded as almost the same as it varies between −1 and −1.4 dB, while and S_B the lowest RL is at −1.7 and −2.7, respectively. Figure 9 shows the experimental and simulated results for all the samples. All the samples show similar trends of decline for the experimental and simulated results, but only brine show an increase in RL with increasing frequency. The values of RL for sandstone and brine were quite high as compared to the sandstone soaked with nanofluids. The wavy plot for experimental results is because of the attenuation of the signal, while for simulated results smooth line was drawn.

4. Conclusion

Simulation results based on FEM show that the RL is minimum in dry sandstone and is maximum when the sandstone was soaked with BFO and ZnO nanofluids. The experimental results from network analyzer show the regular pattern for sandstone soaked in nanofluids, but for dry sandstone, there are some irregularities observed at high frequency. BFO can be regarded as the optimal EOR agent as it shows the highest dielectric permittivity values of 11.55 and 6.59 for real and imaginary parts, respectively. In addition, BFO shows superior permeability values of 1.52 and 1.30 for real and imaginary parts, respectively as compared to ZnO which has values of 1.28 and 0.93 for real and imaginary parts, respectively. Therefore, BFO is beneficial for the sufficient activation of particles with EM waves as it can interact with both magnetic and electric components of EM waves, which can enhance oil recovery. The minimum RL value was observed for sandstone at −38 dB, which matches the simulation results where dry sandstone has minimum RL value, but sandstone saturated with BFO also show impressive RL value of −9.77 dB at higher frequency. BFO can be used as a potential material for EOR because it is the most stable material at the X-band frequency and shows maximum absorption and dielectric permittivity and magnetic permeability values. In the future, BFO can be used as an EOR agent in the presence of electromagnetic field to study the core flooding experiments.

Disclosure statement

No potential conflict of interest was reported by the authors.

Funding

The authors wish to acknowledge the support of Yayasan Universiti Teknologi PETRONAS (YUTP) research grant through cost center 015LC0-143, and Universiti Teknologi Petronas.

ORCID

Hassan Ali http://orcid.org/0000-0001-6040-4347
Hassan Soleimani http://orcid.org/0000-0002-6996-6685
Noorhana Yahya http://orcid.org/0000-0001-9015-8714
Shelley Lorimer http://orcid.org/0000-0002-3962-6380
Maziyar Sabet http://orcid.org/0000-0001-6192-5195
Birol M. R. Demiral http://orcid.org/0000-0003-2055-5452
Lawal Lanre Adebayo http://orcid.org/0000-0001-9456-3944

References

[1] ShamsiJazeyi H, Miller CA, Wong MS, et al. Polymer-coated nanoparticles for enhanced oil recovery. J Appl Polym Sci. 2014;131(15):40576.

[2] Afolabi RO. Enhanced oil recovery for emergent energy demand: challenges and prospects for a nanotechnology paradigm shift. Int Nano Lett. Mar 2019;9(1):1–15. DOI:10.1007/s40089-018-0248-0

[3] Joonaki E, Ghanaatian S. The application of nanofluids for enhanced oil recovery: effects on interfacial tension and coreflooding process. Pet Sci Technol. 2014;32(21):2599–2607.

[4] Sun Q, Li Z, Li S, et al. Utilization of surfactant-stabilized foam for enhanced oil recovery by adding nanoparticles. Energy Fuels. 2014;28(4):2384–2394.

[5] Agista MN, Guo K, Yu Z. A state-of-the-art review of nanoparticles application in petroleum with a focus on enhanced oil recovery (in English). Appl Sci. 2018;8(6): Review:Art no. 871. DOI:10.3390/app8060871

[6] Soleimani H, Baig MK, Yahya N, et al. Synthesis of ZnO nanoparticles for oil–water interfacial tension reduction in enhanced oil recovery. Appl Phys A. 2018;124(2):128.

[7] Majeed A, Zeeshan A, Alamri SZ, et al. Heat transfer analysis in ferromagnetic viscoelastic fluid flow over a stretching sheet with suction. Neural Comput Appl. 2018;30(6):1947–1955.

[8] Zeeshan A, Ellahi R, Mabood F, et al. Numerical study on bi-phase coupled stress fluid in the presence of Hafnium and metallic nanoparticles over an inclined plane. Int J Numer Methods Heat Fluid Flow. 2019;29:2854–2869.

[9] Nikkhah V, Sarafraz M, Hormozi F. Application of spherical copper oxide (II) water nano-fluid as a potential coolant in a boiling annular heat exchanger. Chem Biochem Eng Q. 2015;29(3):405–415.

[10] Soleimani H, Baig MK, Yahya N, et al. Impact of carbon nanotubes based nanofluid on oil recovery efficiency using core flooding. Results Phys. 2018;9:39–48.

[11] Soleimani H, Yahya N, Baig M, et al. Synthesis of carbon nanotubes for oil-water interfacial tension reduction. Oil Gas Res. 2015;1:104.

[12] Maskeen MM, Zeeshan A, Mehmood OU, et al. Heat transfer enhancement in hydromagnetic alumina–copper/water hybrid nanofluid flow over a stretching cylinder. J Therm Anal Calorim 2019;138(2):1127–1136.

[13] Gbadamosi AO, Junin R, Manan MA, et al. Recent advances and prospects in polymeric nanofluids application for enhanced oil recovery. J Ind Eng Chem Oct 2018;66:1–19. DOI:10.1016/j.jiec.2018.05.020

[14] Yahya N, Kashif M, Nasir N, et al. Cobalt ferrite nanoparticles: an innovative approach for enhanced oil recovery application. J. Nano Res. 2012;17:115–126. Trans Tech Publ.

[15] Latiff NRA, Soleimani H, Zaid HM, et al. Magnetoviscous effect of ferrite-based magnetic fluid for EOR application. AIP Conf Proc. 2016;1787(1) AIP Publishing:050021.

[16] Kothari N, Raina B, Chandak KB, et al. Application of ferrofluids for enhanced surfactant flooding in IOR. SPE EUROPEC/EAGE Annual Conference and Exhibition; 2010; Society of Petroleum Engineers.

[17] Esfe MH, Saedodin S, Naderi A, et al. Modeling of thermal conductivity of ZnO-EG using experimental data and ANN methods. Int Commun Heat Mass Transfer. 2015;63:35–40.

[18] Safaei MR, Hajizadeh A, Afrand M, et al. Evaluating the effect of temperature and concentration on the thermal conductivity of ZnO-TiO2/EG hybrid nanofluid using artificial neural network and curve fitting on experimental data. Phys A. 2019;519:209–216.

[19] Nakhjavani M, Nikkhah V, Sarafraz M, et al. Green synthesis of silver nanoparticles using green tea leaves: experimental study on the morphological, rheological and antibacterial behaviour. Heat Mass Transfer. 2017;53(10):3201–3209.

[20] Marin M, Maskeen M, Zeeshan A, et al. Hydromagnetic transport of iron nanoparticle aggregates suspended in water. Indian J Phys. 2019;93(1):53–59.

[21] Ellahi R, Sait SM, Shehzad N, et al. Numerical simulation and mathematical modeling of electro-osmotic Couette–Poiseuille flow of MHD power-law nanofluid with entropy generation. Symmetry (Basel). 2019;11(8):1038.

[22] Hassan M, Fetecau C, Majeed A, et al. Effects of iron nanoparticles' shape on convective flow of ferrofluid under highly oscillating magnetic field over stretchable rotating disk. J Magn Magn Mater. 2018;465:531–539.

[23] Majeed A, Zeeshan A, Noori FM, et al. Influence of rotating magnetic field on Maxwell saturated ferrofluid flow over a heated stretching sheet with heat generation/absorption. Mech Ind. 2019;20(5):502.

[24] Sarafraz M, Pourmehran O, Yang B, et al. Pool boiling heat transfer characteristics of iron oxide nanosuspension under constant magnetic field. Int J Therm Sci. 2020;147:106131.

[25] Anantharaman M, Malini KA, Sindhu S, et al. Tailoring magnetic and dielectric properties of rubber ferrite composites containing mixed ferrites. Bull Mater Sci. 2001;24(6):623–631.

[26] Qi X, Zhou J, Yue Z, et al. A ferroelectric ferromagnetic composite material with significant permeability and permittivity. Adv Funct Mater. 2004;14(9):920–926.

[27] Ellahi R, Zeeshan A, Shehzad N, et al. Structural impact of Kerosene-Al2O3 nanoliquid on MHD Poiseuille flow with variable thermal conductivity: application of cooling process. J Mol Liq. 2018;264:607–615.

[28] Salari E, Peyghambarzadeh SM, Sarafraz MM, et al. Boiling thermal performance of TiO2 aqueous nanofluids as a coolant on a disc copper block. Periodica Polytechnica Chem Eng. 2016;60(2):106–122.

[29] Nikkhah V, Sarafraz M, Hormozi F, et al. Particulate fouling of CuO–water nanofluid at isothermal diffusive condition inside the conventional heat exchanger-experimental and modeling. Exp Therm Fluid Sci. 2015;60:83–95.

[30] Spaldin NA. Multiferroics: past, present, and future. MRSBU. 2017;42(5):385–390.

[31] Jiang W, Jiang C, Gong X, et al. Structure and electrorheological properties of nanoporous BaTiO 3 crystalline powders prepared by sol–gel method. JSGST. 2009;52(1):8–14.

[32] Soleimani H, Ahmad Latiff NR, Yahya N, et al. Effect of annealing temperature on the crystallization of Hematite-Alumina (Fe2O3-Al2O3) nanocomposite and Its influence in EOR application. J. Nano Res. 2014;29: 105–113: Trans Tech Publ.

[33] Divandari H, Hemmati-Sarapardeh A, Schaffie M, et al. Integrating synthesized citric acid-coated magnetite nanoparticles with magnetic fields for enhanced oil recovery: experimental study and mechanistic understanding. J Petroleum Sci Eng. 2019;174:425–436.

[34] Sarafraz M, Hormozi F. Intensification of forced convection heat transfer using biological nanofluid in a double-pipe heat exchanger. Exp Therm Fluid Sci. 2015;66:279–289.

[35] Bera A, Belhaj H. Application of nanotechnology by means of nanoparticles and nanodispersions in oil recovery-A comprehensive review. J Nat Gas Sci Eng. 2016;34:1284–1309.
[36] Almahfood M, Bai B. The synergistic effects of nanoparticle-surfactant nanofluids in EOR applications (in English). J Petroleum Sci Eng. 2018;171:196–210; Review. DOI:10.1016/j.petrol.2018.07.030
[37] Ahmed Z, Nadeem S, Saleem S, et al. Numerical study of unsteady flow and heat transfer CNT-based MHD nanofluid with variable viscosity over a permeable shrinking surface. Int J Numer Methods Heat Fluid Flow. 2019;29:4607–4623.
[38] Ellahi R, Alamri SZ, Basit A, et al. Effects of MHD and slip on heat transfer boundary layer flow over a moving plate based on specific entropy generation. J Taibah Univ Sci. 2018;12(4):476–482.
[39] Danlée Y, Bailly C, Huynen I. Thin and flexible multilayer polymer composite structures for effective control of microwave electromagnetic absorption. Compos Sci Technol. 2014;100:182–188.
[40] Goodarzi M, Toghraie D, Reiszadeh M, et al. Experimental evaluation of dynamic viscosity of ZnO–MWCNTs/engine oil hybrid nanolubricant based on changes in temperature and concentration. J Therm Anal Calorim 2019;136(2):513–525.
[41] Qiu J, Wu X, Qiu T. High electromagnetic wave absorbing performance of activated hollow carbon fibers decorated with CNTs and Ni nanoparticles. Ceram Int. 2016;42(4):5278–5285.
[42] Zhang X, Donga XL, Huang H, et al. Microwave absorption properties of the carbon-coated nickel nanocapsules. Appl Phys Lett. 2006;89(5):053115.
[43] Adebayo LL, Soleimani H, Yahya N, et al. Investigation of the broadband microwave absorption of citric acid coated Fe3O4/PVDF composite using finite element method. Appl Sci. 2019;9(18):3877.
[44] Kadlec R, Fiala P, Nešpor D. Electromagnetic wave propagation in heterogeneous structures. PIERS Online. 2010;6(7):613–616.
[45] Adil M, Zaid HM, Chuan LK, et al. Effect of dispersion stability on electrorheology of water-based ZnO nanofluids. Energy Fuels. 2016;30(7):6169–6177.
[46] Nikoofar K, Haghighi M, Lashanizadegan M, et al. Zno nanorods: efficient and reusable catalysts for the synthesis of substituted imidazoles in water. J Taibah Univ Sci. 2015;9(4):570–578.
[47] Bolarinwa H, Onuu MU, Fasasi AY, et al. Determination of optical parameters of zinc oxide nanofibre deposited by electrospinning technique. J Taibah Univ Sci. 2017;11(6):1245–1258.
[48] Adebayo LL, Soleimani H, Yahya N, et al. Recent advances in the development OF Fe3O4-BASED microwave absorbing materials. Ceram Int 2020;46(2):1249–1268. DOI:10.1016/j.ceramint.2019.09.209
[49] Ansari SA, Nisar A, Fatma B, Khan W, et al. Temperature dependence anomalous dielectric relaxation in Co doped ZnO nanoparticles. Mater Res Bull. 2012;47(12):4161–4168.
[50] Alizadeh S, Mani A. Multiscale model for electrokinetic transport in networks of pores, part I: model derivation (in English). Langmuir. Jun 27 2017;33(25):6205–6219. DOI:10.1021/acs.langmuir.6b03816
[51] Ali H, Soleimani H, Yahya N, et al. Finite element method for modelling of two phase fluid flow in porous media. J Phys Conf Ser. 2018;1123(1):012002.
[52] Wahaab FA, Yahya N, Shafie A, et al. Determination of optimum frequency for electromagnetic-assisted nanofluid core flooding. Appli Sci. 2019;9(21):4608.
[53] Deng Y, Korvink JG. Topology optimization for three-dimensional electromagnetic waves using an edge element-based finite-element method. Proc R Soc A Math Phys Eng Sci. 2016;472(2189):20150835.
[54] Aldridge DF. Reflection and transmission of plane electromagnetic waves by a geologic layer. Technical Report SAND2017-3657, Sandia National Laboratories, US Department . . . ; 2017.
[55] Costa F, Borgese M, Degiorgi M, et al. Electromagnetic characterisation of materials by using transmission/reflection (T/R) devices. Electronics (Basel). 2017;6(4):95.
[56] Hallbjorner P. The significance of radiation efficiencies when using S-parameters to calculate the received signal correlation from two antennas. IEEE Antennas Wirel Propag Lett. 2005;4(1):97–99.
[57] Sun J, Huang M, Peng J, et al. The simulation of the frequency-dependent effective permittivity for composite materials. Proceedings of the 9th International Symposium on Antennas, propagation and EM theory; 2010; IEEE. p. 701–704.